



HAL
open science

Coupled heat transfers resolution by Monte Carlo in urban geometry including direct and diffuse solar irradiations

Cyril Caliot, Louis d'Alençon, Stéphane Blanco, Vincent Forest, Richard Fournier, Frédéric Hourdin, Florent Retailleau, Robert Schoetter, Najda Villefranque

► **To cite this version:**

Cyril Caliot, Louis d'Alençon, Stéphane Blanco, Vincent Forest, Richard Fournier, et al.. Coupled heat transfers resolution by Monte Carlo in urban geometry including direct and diffuse solar irradiations. *International Journal of Heat and Mass Transfer*, 2024, 222, pp.125139. <10.1016/j.ijheatmasstransfer.2023.125139>. <hal-04387332v2>

HAL Id: hal-04387332

<https://hal.science/hal-04387332v2>

Submitted on 16 Jan 2024

HAL is a multi-disciplinary open access archive for the deposit and dissemination of scientific research documents, whether they are published or not. The documents may come from teaching and research institutions in France or abroad, or from public or private research centers.

L'archive ouverte pluridisciplinaire **HAL**, est destinée au dépôt et à la diffusion de documents scientifiques de niveau recherche, publiés ou non, émanant des établissements d'enseignement et de recherche français ou étrangers, des laboratoires publics ou privés.

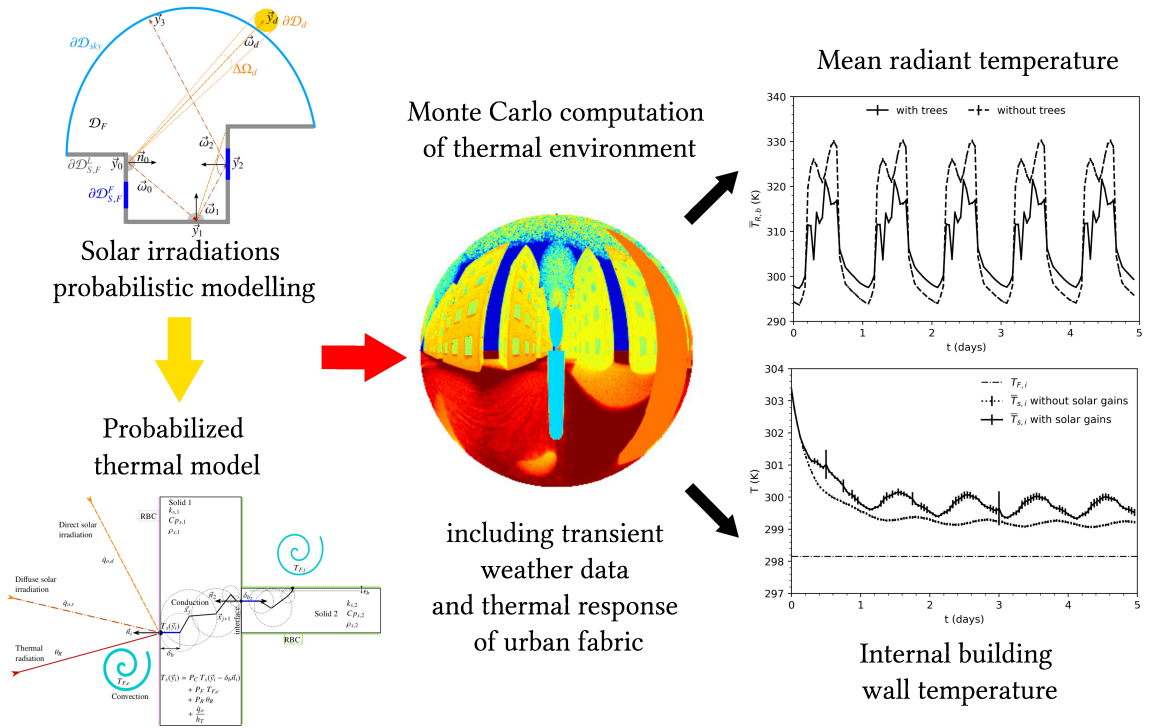


HAL Authorization

Graphical Abstract

Coupled heat transfers resolution by Monte Carlo in urban geometry including direct and diffuse solar irradiations

Cyril Caliot, Louis d'Alençon, Stéphane Blanco, Vincent Forest, Richard Fournier, Frédéric Hourdin, Florent Retailleau, Robert Schoetter, Najda Villefranque



Coupled heat transfers resolution by Monte Carlo in urban geometry including direct and diffuse solar irradiations

Cyril Caliot^{a,*}, Louis d'Alençon^b, Stéphane Blanco^c, Vincent Forest^d, Richard Fournier^c, Frédéric Hourdin^b, Florent Retailleau^a, Robert Schoetter^e, Najda Villefranque^b

^a*CNRS, UPPA, E2S, LMAP, 1 Allée du Parc Montaury, 64600, Anglet, France.*

^b*LMD/IPSL/SU, CNRS, Paris, France.*

^c*Laplace, INP/Université de Toulouse/CNRS, Toulouse, France.*

^d*Méso-Star, Longages, France.*

^e*CNRM, Université de Toulouse, Météo-France, CNRS, Toulouse, France.*

Abstract

Modelling transient combined heat transfer in complex urban geometry is a key step to predict human exposure or energy consumption and to quantify the effect of climate change mitigation and adaptation measures. A difficulty lies in the possibility for a model to scale up and integrate large and complex urban morphology. We develop a probabilistic approach to solve heat transfers with the Monte Carlo method that is insensitive to the complexity of both the urban geometry and the boundary conditions. The integral formulation that includes random walks for each heat transfer mode is presented and the computation of absorbed solar irradiations at walls with the double randomization technique is detailed. Numerical validations are given through comparisons with deterministic method results for single and two-layer slabs, but also a three-dimensional thermal bridge geometry. The developed probabilistic heat transfer model is then used in a demonstration heat wave scenario where are computed: the outdoor mean radiant temperature showing the influence of trees; and the indoor average wall temperature showing the influence of solar gains through windows.

Keywords: Coupled heat transfer, Monte Carlo, Solar irradiation, Indoor and outdoor human thermal comfort, Building energy consumption, Thermal inertia

*Corresponding author

Email address: cyril.caliot@cnrs.fr (Cyril Caliot)

1. Introduction

Human health [1] and energy consumption [2] are affected by the city microclimate, specifically during heat waves where their impacts are enhanced by the local climate change associated to a growing urbanization and population density [3]. Adaptation measures should be found to avoid vulnerability to extreme heat by limiting urban temperature rise and improving resilience of the city fabric. Numerical evaluations of such adaptation measures represent a difficult task requiring to consider the atmospheric boundary layer and the city complexity where heat and mass transfers are strongly coupled between a large diversity of materials and spatio-temporal scales [4, 5].

To tackle this challenge, physical deterministic (mesh-based) models have been developed that may be classified in three complementary families covering different spatio-temporal scales: (1) Urban canopy models [6] simulate the urban surface energy balance assuming a simplified urban geometry (e.g., an infinitely-long street canyon [7]) in numerical weather prediction, regional and global climate models [8]; (2) Urban microclimate models associated with building energy models are used to predict building performances [9] and outdoor pedestrian thermal comfort [10]; (3) Heat transfer models (e.g., finite volume or finite element methods) are used to evaluate or optimize building envelopes [11] and component thermal performances [12]. Characteristic space and time increments decrease from first to third family and the most refined results are used to develop and validate coarser approximate models. This upscaling methodology is subjected to approximations or parametrizations hypothesis which may be validated by experimental measurements presenting increasing uncertainties with the spatio-temporal scales. Thus, there is a lack of numerical methods that support accurately the scaling up and can be applied on this range of scales (i.e., from mm to m and km) to numerically validate the assumptions and parametrizations.

Although it is well-known that the Monte Carlo method (MCM) [13] can solve linear integrals whatever the domain size and number of dimensions, it has only recently been foreseen to solve for the temperature with a single MCM algorithm where conduction-radiation-convection [14] are coupled. Early studies at steady-state [15, 16] and transient [17] regimes have demonstrated the ability of MCM algorithms to solve for conductive, advective and radiative heat transfers in three-dimensional porous media with opaque solid surfaces and transparent fluid subdomains. Indeed, the heat transfer equation in a solid, with Robin's boundary condition (RBC), has been coupled to the radiative transfer equation (RTE) through the double randomization technique (DRT) [18] allowing one to build conduction-advection-radiation random paths represented as broken lines linking the sources to a probe calculation point. Although, the physical concepts are well established, it is very recently that the theoretical framework was exposed by Tregan et al. [19] in case of transient heat transfer in adjacent semi-transparent fluid and solid subdomains.

Tregan et al. [19] established the probabilistic thermal model in linear situations when the Green's functions are known, that includes a recursive coupling of each heat transfer mode. This approach was also generalized to unknown propagators by translating each heat transfer mode into stochastic processes and using Feynman-Kac's formula. The same recursive structure was found for the probabilistic heat transfer mode couplings. Moreover, using the same framework in steady-state regime, Ibarrart et al. [20, 16] added the resolution of advective heat transfer in fluid subdomains enclosed by opaque solids. They also demonstrated that the MCM approach was insensitive to the geometry size. Indeed, this new approach has benefited practically from the computer graphics advances in image synthesis with MCM techniques [21] by the public release of efficient free software which guaranty independence between the MCM algorithm and the complex data representation while insuring fast access to data and the ability to manage large and complex three-dimensional (3D) geometry [22]. In addition, Penazzi et al. [23] showed that the MCM algorithms developed to solve coupled heat transfers may be used to estimate and store propagators when heterogeneous and transient sources are known. This enables re-using propagators to evaluate their corresponding probe temperatures when the sources are different leading to a drastic reduction of computation time. However, in the specific application of urban physics, the outdoor and indoor absorbed solar irradiances are unknown sources that originate from direct and diffuse solar irradiances but also from multiple reflections within the complex geometry. Thus, to solve coupled heat transfers in urban environments with a single MCM algorithm that is insensitive to geometrical refinements, the existing theoretical framework [19, 20, 23] should be enriched with a model for solar sources and their coupling to thermal heat transfers.

The purpose of this article is to present a new probabilistic model based on the theoretical framework of Tregan et al. [19] to solve linearized transient conduction-radiation problems with RBC in complex 3D urban geometry including Lambertian and specular surfaces where solar irradiances are unknown and need to be calculated with MCM. Only sensible heat transfer through solids is considered and not the one originating from moisture heat and mass transfer [24]. Nevertheless, the proposed model will allow one to consider new scientific questions by unlocking the feasibility of new simulations in complex and large urban geometry. To illustrate the model capabilities, a heat wave scenario is chosen as a demonstration case where key variables of the outdoor human thermal comfort and building energy consumptions are computed accounting for detailed tree geometry or indoor solar gains.

In Sect. 2, the MCM algorithm involving the mixed random walks is presented with a detailed description of the solar flux density management at urban geometry walls. Section 3 gathers the 1D and 3D numerical validations and Sect. 4 demonstrates the ability of the proposed model to compute temperatures involved in the evaluation of outdoor comfort

and energy consumption during a heat wave scenario.

2. Probabilizing coupled heat-transfer and solving with a Monte Carlo algorithm

The goal of the present heat transfer model (HTM) is to compute:

- either a probe temperature for a solid material in an urban environment, where the probe temperature may be defined as the solid temperature at a specific location or as a surface or volume average temperature;
- or an infrared radiance temperature, i.e. the intensity of radiation at a given location in a given direction, spectrally integrated over the whole infrared.

In this model, transient conductive heat transfer (Eq. 1a) is considered inside each of the solid parts of the system (e.g., walls, windows, ground). They are divided into subparts where the solid properties are uniform and isotropic. As far as radiation is concerned, solid media are either transparent or opaque (no semi-transparent media). Each solid sub-part S is defined as occupying a domain \mathcal{D}_S . At the initial time τ_I the solid is isothermal within each sub-part at a temperature noted T_I (Eq. 1b). The boundary of \mathcal{D}_S is noted $\partial\mathcal{D}_S$ and is potentially split into three parts: solid-solid ($\partial\mathcal{D}_{S,S}$) or solid-fluid ($\partial\mathcal{D}_{S,F}$) interfaces, and parts with a Dirichlet boundary condition ($\partial\mathcal{D}_{S,D}$). For the Dirichlet boundary conditions, the boundary temperature is known and is noted T_D (Eq. 1c). On $\partial\mathcal{D}_{S,S}$, the model for the interface is flux continuity, i.e. equalling the conductive fluxes in the two adjacent solids (Eq. 1d). On $\partial\mathcal{D}_{S,F}$, the model for the interface is also a flux continuity, this time equalling the conductive flux inside the solid with the sum of the convective and radiative fluxes on the fluid part, leading to a Robin boundary condition (RBC, Eq. 1e).

$$\left\{ \begin{array}{ll} \frac{\partial}{\partial t} T_s(\vec{x}, t) = \alpha \Delta T_s(\vec{x}, t), & \vec{x} \in \mathcal{D}_S, t > \tau_I, \quad (1a) \\ T_s(\vec{x}, t) = T_I, & \vec{x} \in \mathcal{D}_S \cup \partial\mathcal{D}_S, t \leq \tau_I, \quad (1b) \\ T_s(\vec{y}, t) = T_D(\vec{y}, t), & \vec{y} \in \partial\mathcal{D}_{S,D}, t > \tau_I, \quad (1c) \\ k_{s,1} \nabla T_s(\vec{y}, t) \cdot \vec{n}_1 = k_{s,2} \nabla T_s(\vec{y}, t) \cdot \vec{n}_2, & \vec{y} \in \partial\mathcal{D}_{S,S}, t > \tau_I, \quad (1d) \\ k_s \nabla T_s(\vec{y}, t) \cdot \vec{n} = \dot{q}_F(\vec{y}, t) + \dot{q}_R(\vec{y}, t) + \dot{q}_o(\vec{y}, t), & \vec{y} \in \partial\mathcal{D}_{S,F}, t > \tau_I, \quad (1e) \end{array} \right.$$

where $\alpha = \frac{k_s}{\rho_s C_{p,s}}$ is the solid thermal diffusivity; k_s , the thermal conductivity; ρ_s , the density; $C_{p,s}$, the specific heat capacity; \vec{n} , the local outward normal (subscripts 1 and 2 stand for two adjacent solids in perfect contact). The RBC (Eq. 1e) includes \dot{q}_F , the rate of heat transfer by convection, \dot{q}_R , the net exchange rate of heat transfer by thermal radiation

(linearized), and \dot{q}_o , the absorbed solar irradiation that is the sum of the direct ($\dot{q}_{o,d}$) and diffuse ($\dot{q}_{o,r}$) solar irradiations.

$$\dot{q}_F(\vec{y}, t) = h_F(\vec{y}, t) [T_F(\vec{y}, t) - T_s(\vec{y}, t)], \quad (2)$$

$$\dot{q}_R(\vec{y}, t) = h_R(\vec{y}) [\theta_R(\vec{y}, t) - T_s(\vec{y}, t)], \quad (3)$$

$$\dot{q}_o(\vec{y}, t) = \int_0^{+\infty} d\lambda \int_{2\pi} d\Omega(\vec{\omega}) |\vec{\omega} \cdot \vec{n}| \varepsilon(\vec{y}, \lambda) I_o(\vec{y}, t, -\vec{\omega}, \lambda). \quad (4)$$

The expression of \dot{q}_F (Eq. 2) is given by the Newton's Law of Cooling involving the heat transfer coefficient by convection h_F and a homogeneous fluid (air) temperature T_F . Two types of fluid temperature will be considered. The first one corresponds to the atmospheric air temperature surrounding the buildings and provided by meteorological data, $T_F \equiv T_{F,e}$. The second one is the temperature of the fluid inside an enclosure (closed habitation room) assumed perfectly stirred, $T_F \equiv T_{F,i}$. Although an additional model may be formulated to compute $T_{F,i}$, such as a function of a given heating system inside each room, these room air temperatures are assumed known in this study. \dot{q}_R (Eq. 3) is formulated with an expression similar to Eq. 2 but the radiative temperature, θ_R , is unknown. Indeed, after a linearization of the net exchange rate of thermal radiation between the surface and its environment, Eq. 3 is obtained that includes the radiative temperature, θ_R , which is the integral of the radiance temperature over the hemisphere solid angles. For conciseness, the derivation of Eq. 3 and the integral formulation of θ_R is not replicated but may be found in the work of Penazzi et al. [23] and Bati et al. [25] (and also in Tregan et al. [19] for semi-transparent media). The absorbed solar irradiation is also unknown and its expression is given in Eq. 4 involving the unknown incident solar radiative intensity I_o . To compute \dot{q}_R and \dot{q}_o the RTE, Eq. 5a, and its boundary condition, Eq. 5b, should be solved in transparent media (\mathcal{D}_F) between opaque surfaces:

$$\left\{ \begin{array}{l} \vec{\omega}_i \cdot \nabla I(\vec{x}, \vec{\omega}_i, \lambda) = 0, \\ I(\vec{y}_i, -\vec{\omega}_i, \lambda) = \varepsilon(\vec{y}_{i+1}, -\vec{\omega}_i, \lambda) I_b(\vec{y}_{i+1}, \lambda) + \\ \int_{2\pi} d\Omega(\vec{\omega}_{i+1}) \rho''(\vec{y}_{i+1}, -\vec{\omega}_i | -\vec{\omega}_{i+1}, \lambda) \times \\ |\vec{\omega}_{i+1} \cdot \vec{n}_{i+1}| I(\vec{y}_{i+1}, -\vec{\omega}_{i+1}, \lambda), \end{array} \right. \quad \begin{array}{l} \vec{x} \in \mathcal{D}_F, \\ \vec{y} \in \partial\mathcal{D}_{S,F}. \end{array} \quad (5a)$$

$$\left\{ \begin{array}{l} \vec{\omega}_i \cdot \nabla I(\vec{x}, \vec{\omega}_i, \lambda) = 0, \\ I(\vec{y}_i, -\vec{\omega}_i, \lambda) = \varepsilon(\vec{y}_{i+1}, -\vec{\omega}_i, \lambda) I_b(\vec{y}_{i+1}, \lambda) + \\ \int_{2\pi} d\Omega(\vec{\omega}_{i+1}) \rho''(\vec{y}_{i+1}, -\vec{\omega}_i | -\vec{\omega}_{i+1}, \lambda) \times \\ |\vec{\omega}_{i+1} \cdot \vec{n}_{i+1}| I(\vec{y}_{i+1}, -\vec{\omega}_{i+1}, \lambda), \end{array} \right. \quad \begin{array}{l} \vec{x} \in \mathcal{D}_F, \\ \vec{y} \in \partial\mathcal{D}_{S,F}. \end{array} \quad (5b)$$

with ρ'' the reciprocal bidirectional reflection distribution function (BRDF), ε the material directional emissivity, and I_b the Planck's law of blackbody radiative intensity. The numbering of the positions and directions follows a reverse radiative path as depicted in Fig. 1b. Most of the surfaces are considered Lambertian ($\mathcal{D}_{S,F}^L$, Eq. 7) and some are assumed specular ($\mathcal{D}_{S,F}^F$, Eq. 8) to represent window glasses. In addition, the BRDF may be

expressed as the product of an angular function (f_ρ) and a reflection probability (P_ρ):

$$\rho''(\vec{y}_{i+1}, -\vec{\omega}_i | -\vec{\omega}_{i+1}, \lambda) = f_\rho(\vec{y}_{i+1}, -\vec{\omega}_i | -\vec{\omega}_{i+1}, \lambda) P_\rho(\vec{y}_{i+1}, -\vec{\omega}_{i+1}, \lambda), \quad (6)$$

$$\rho''_L(\vec{y}_{i+1}, \lambda) = \frac{1}{\pi} \rho^{\cap\cap}(\vec{y}_{i+1}, \lambda), \quad (7)$$

$$\rho''_F(\vec{y}_{i+1}, -\vec{\omega}_i | -\vec{\omega}_{i+1}, \lambda) = \frac{\delta(\vec{\omega}_{i+1} - \vec{R}(-\vec{\omega}_i, \vec{n}_{i+1}))}{|\vec{\omega}_{i+1} \cdot \vec{n}_{i+1}|} F(\vec{y}_{i+1}, -\vec{\omega}_{i+1}, \lambda), \quad (8)$$

$$P_\rho(\vec{y}_{i+1}, -\vec{\omega}_{i+1}, \lambda) = \begin{cases} \rho^{\cap\cap}(\vec{y}_{i+1}, \lambda), & \text{for Lambertian surfaces,} \\ F(\vec{y}_{i+1}, -\vec{\omega}_{i+1}, \lambda), & \text{for specular surfaces,} \end{cases} \quad (9)$$

where $\rho^{\cap\cap}$ is the hemispherical-hemispherical reflectivity, δ is the Dirac's delta function, \vec{R} is the specular direction, and F is the Fresnel reflectivity dependent on the incident direction. The resolution of the presented HTM requires to solve for the HTE (Eqs. 1a-1e) coupled to resolutions of RTE (Eqs. 5a-5b) for thermal and solar radiative heat transfer. Tregan et al [19] have shown that a probe computation of the solid temperature by MCM may be done through the sampling of heat paths that explores the domain backward in time until reaching a known source. If $T_s(\vec{y}_0, t_0)$ is the quantity to estimate (with $\vec{y}_0 \in \partial\mathcal{D}_{S,F}$ and $t_0 > \tau_I$), the MCM algorithm will draw N realizations of the MCM weight W_k to build an estimate \tilde{T}_s of T_s and its associated standard error:

$$T_s(\vec{y}_0, t_0) \approx \tilde{T}_s(\vec{y}_0, t_0) = \frac{1}{N} \sum_{k=1}^N W_k,$$

$$\tilde{\sigma}_{\tilde{T}_s} = \frac{1}{\sqrt{N}} \sqrt{\frac{1}{N} \sum_{k=1}^N W_k^2 - \tilde{T}_s^2(\vec{y}_0, t_0)}.$$

The approach adopted by Tregan et al [19] and Penazzi et al [23] leads to follow mixed random walks including conductive and radiative sub-paths until a known temperature is reached and accounting for known surface or volume flux densities along the paths. Indeed, conductive sub-paths were followed with a δ -sphere technique and the radiative sub-paths were tracked with standard ray-tracing. An important step of the approach is the probabilization of RBC, Eq. 1e, that makes possible the connection of sub-paths:

$$T_s(\vec{y}, t) = P_C T_s(\vec{y} - \delta_b \vec{n}, t) + P_F T_F(\vec{y}, t) + P_R \theta_R(\vec{y}, t) + \frac{\dot{q}_o(\vec{y}, t)}{h_T}, \quad \vec{y} \in \partial\mathcal{D}_{S,F}, \quad t > \tau_I, \quad (10)$$

where δ_b is the reinjection length ([19, 23]), P_C , P_F and P_R are probabilities associated respectively to the contribution of conduction, convection and radiation:

$$P_C(\vec{y}_i, t) = \frac{k_s(\vec{y}_i, t)}{\delta_b h_T(\vec{y}_i, t)}, \quad P_F(\vec{y}_i, t) = \frac{h_F(\vec{y}_i, t)}{h_T(\vec{y}_i, t)}, \quad P_R(\vec{y}_i, t) = \frac{h_R(\vec{y}_i, t)}{h_T(\vec{y}_i, t)},$$

$$h_T(\vec{y}, t) = \frac{k_s(\vec{y}, t)}{\delta_b} + h_F(\vec{y}, t) + h_R(\vec{y}, t).$$

The last term of Eq. 10 is unknown and involves the absorption of solar radiation by the solid surface. For a known local flux density on solid surfaces, Penazzi et al [23] accounted for it by increasing the MCM weight with its values, each time the interface is visited by the random walk. In this study, we use DRT to account for the unknown solar flux absorption at RBC surfaces. Thus, each time a RBC is visited by the random walk, only one realization of $\frac{\dot{q}_o(\vec{y}, t)}{h_T}$ is accounted for and increases the MCM weight by a quantity $W_{o,k}$. Thus, the MCM weight may be formulated as:

$$W_k(\vec{y}_0, t_0) = H(t_n \leq \tau_I) T_I + H(t_n > \tau_I) \left\{ H(\vec{y}_n \in \partial\mathcal{D}_{S,D}) T_D(\vec{y}_n, t_n) + \right. \\ \left. H(\vec{y}_n \in \partial\mathcal{D}_{S,F}) T_F(\vec{y}_n, t_n) + H(\vec{y}_n \in \partial\mathcal{D}_{sky}) T_{sky}(\vec{y}_n, \vec{\omega}_n, t_n) \right\} + W_{o,k}, \quad (11)$$

with n the index at path end after n jumps of the random walk (conductive and radiative), and $H(\cdot)$ is a test function. Its value is unity if the condition is fulfilled and zero otherwise. In Eq. 11, the first test is used to manage the initial condition. Indeed, at the end of the k th path, a known temperature has been reached. If the conductive path, that goes back in time, reaches τ_I , the first test function is unity, and zero otherwise. If the initial time is not reached, then additional tests are involved in Eq. 11 to identify where the path ends: at a solid boundary (Eq. 1c), in the fluid or in the sky. The full algorithm flowchart associated with each MCM realization is depicted in Fig. 2 and includes possible starting points (inside the solid, at an interface, or from a camera), the conditional steps with the recorded solar flux densities along the conduction-radiation random path and the temperatures at path ends. At an interface having a RBC ($\partial\mathcal{D}_{S,F}$), the MCM algorithm will sample a realization of the interface temperature (Eq. 10) based on the probabilities, i.e., T_C , T_F , or θ_R . This sampling is done by comparing the probabilities P_C , P_F and P_R to a random number R , uniformly distributed between 0 and 1, and generated by the pseudo-random number generator ThreeFry [26]. If T_F is sampled, the MCM algorithm stops because the fluid temperature is assumed known. In the other cases, DRT allows us to evaluate the unknown temperature by starting a conductive or radiative path. If $T_s(\vec{y}_i - \delta_b \vec{n}_i, t)$

is sampled, a conductive sub-path is started at $\vec{y}_i - \delta_b \vec{n}_i$ (see Fig. 1a). In the developed model, the floating random walk-on-sphere (WOS) technique is used for the conductive random walk with an absorbing thickness parameter ϵ_b [27, 28]. Alternatively, if $\theta_R(\vec{y}_i, t)$ is required, the random walk is followed with a multiple reflection path (ray-tracing) in the urban geometry. As previously stated, the absorbed solar flux is evaluated with DRT leading to start a sub-path for $\dot{q}_{o,d}$ and another one for $\dot{q}_{o,r}$. Figure 1a presents the paths belonging to different heat transfer modes and starting at a wall boundary with a RBC. The next paragraphs present the integral formulation for the solar fluxes leading to the expression of $W_{o,k}$.

2.1. Absorbed solar irradiation

The integral formulation of \dot{q}_o is best solved with a MCM algorithm [13] that accounts for multiple reflections as well as spectral and directional optical properties [29, 30]. In the presence of Lambertian surfaces, an improvement of the MCM algorithm convergence may be reached by adopting a splitting of the solar radiative intensity:

$$I_o(\vec{y}_0, -\vec{\omega}_0, \lambda) = I_{o,d}(\vec{y}_0, -\vec{\omega}_0, \lambda) + I_{o,r}(\vec{y}_0, -\vec{\omega}_0, \lambda), \quad (12)$$

with $I_{o,d}$ the radiative intensity coming directly from the Sun without any change of direction and $I_{o,r}$ the radiative intensity of the solar radiation being scattered or reflected at least once. The solar irradiation absorbed is then split into two components, direct ($\dot{q}_{o,d}$) and diffuse ($\dot{q}_{o,r}$):

$$\dot{q}_{o,d}(\vec{y}_0, t) = \int d\lambda \int_{\Delta\Omega_d} d\Omega(\vec{\omega}_d) |\vec{\omega}_d \cdot \vec{n}_0| \varepsilon(\vec{y}_0, \lambda) H(\vec{y}_d \in \partial\mathcal{D}_d) I_{o,d}(\vec{y}_0, -\vec{\omega}_d, \lambda), \quad (13)$$

$$\begin{aligned} \dot{q}_{o,r}(\vec{y}_0, t) = \int d\lambda \int_{2\pi} d\Omega(\vec{\omega}_0) |\vec{\omega}_0 \cdot \vec{n}_0| \varepsilon(\vec{y}_0, \lambda) & \left(H(\vec{y}_1 \in \partial\mathcal{D}_{sky}) I_{o,sky}(\vec{y}_1, -\vec{\omega}_0, \lambda) \right. \\ & \left. + H(\vec{y}_1 \in \partial\mathcal{D}_{S,F}) I_{o,r}(\vec{y}_1, -\vec{\omega}_0, \lambda) \right), \end{aligned} \quad (14)$$

where $\Delta\Omega_d$ is the Sun's solid angle and with the following recursive expression of the diffuse solar intensity,

$$I_{o,r}(\vec{y}_{i+1}, -\vec{\omega}_i, \lambda) = \int_{2\pi} d\Omega(\vec{\omega}_{i+1}) |\vec{\omega}_{i+1} \cdot \vec{n}_{i+1}| \rho''(\vec{y}_{i+1}, -\vec{\omega}_i | -\vec{\omega}_{i+1}, \lambda) I_o(\vec{y}_{i+1}, -\vec{\omega}_{i+1}, \lambda). \quad (15)$$

Figure 1b shows, at point \vec{y}_0 , a direct contribution from the Sun ($\partial\mathcal{D}_d$) in direction $\vec{\omega}_d$ inside the Sun's solid angle $\Delta\Omega_d$. The expression of $\dot{q}_{o,r}$ includes the solar radiation resulting from multiple scatterings in the atmosphere and from multiple reflections by the urban opaque surfaces (see Fig. 1b).

2.2. Absorbed direct solar irradiation

The direct normal irradiation, D_o , is the direct solar radiative flux density incident on a surface oriented perpendicularly to the Sun's centre direction ($\vec{n} \equiv \vec{\omega}_{Sun}$):

$$D_o(\vec{y}) = \int d\lambda \int_{\Delta\Omega_d} d\Omega(\vec{\omega}_d) |\vec{\omega}_d \cdot \vec{n}| I_{o,d}(\vec{y}, -\vec{\omega}_d, \lambda).$$

The Sun's solid angle being small, $I_{o,d}$ is assumed constant in $\Delta\Omega_d$. Thus, an integral formulation of $\dot{q}_{o,d}$, that can be solved with a reverse MCM algorithm, may be given by:

$$\dot{q}_{o,d}(\vec{y}_0, t) = \int p_{N_o}(\lambda) d\lambda \int_{\Delta\Omega_d} p_{\Omega_d}(\vec{\omega}_d) d\Omega(\vec{\omega}_d) W_{o,d}(\vec{y}_0), \quad (16)$$

$$W_{o,d}(\vec{y}_0) = H(\vec{y}_d \in \partial\mathcal{D}_d) \varepsilon(\vec{y}_0) |\vec{\omega}_d \cdot \vec{n}_0| D_o(\vec{y}_0). \quad (17)$$

The MCM weight $W_{o,d}$ (Eq. 17) includes a test that determines the shadowing from direct solar radiation. Equation 16 is formulated with probability density functions (PDF) that are used for the spectral and directional samplings:

$$p_{\Omega_d}(\vec{\omega}_d) = \frac{1}{\Delta\Omega_d}, \quad p_{N_o}(\lambda) = \frac{\varepsilon(\vec{y}_0, \lambda)}{\varepsilon(\vec{y}_0)} p_{\Lambda_o}(\lambda), \quad p_{\Lambda_o}(\lambda) = \frac{I_{o,d}(\vec{y}_0, \lambda)}{I_{o,d}(\vec{y}_0)}.$$

2.3. Absorbed diffuse solar irradiation

The diffuse solar irradiation includes the multiple reflections of the direct Sun's radiation and the sky solar radiation (see Fig. 1b). The multiple scattered solar radiation in the atmosphere is assumed known and given by a solar sky model (e.g., the all-weather sky model from Perez et al. [31]) defining spectral and directional solar intensities $I_{o,sky}$ coming from the sky ($\partial\mathcal{D}_{sky}$). To simplify the formulation, the sky diffuse solar radiative intensity is assumed to have the same spectral behaviour as the solar direct radiative intensity. This leads to separate its spectral and directional dependency: $I_{o,sky}(\vec{\omega}, \lambda) \equiv f_{sky}(\vec{\omega}) I_{o,d}(\lambda)$. Then, Eq. 14 may be reformulated,

$$\dot{q}_{o,r}(\vec{y}_0, t) = \int p_{N_o}(\lambda) d\lambda \int_{2\pi} p_{\Omega}(\vec{\omega}_0) d\Omega(\vec{\omega}_0) \left(W_{o,sky} + H(\vec{y}_1 \in \partial\mathcal{D}_{S,F}) W_{o,r}(\vec{y}_1, -\vec{\omega}_0, \lambda) \right) \quad (18)$$

Expressing the BRDF with Eq. 6 and using the solar intensity splitting (Eq. 12) for Lambertian surfaces only, the recursive term accounting for the multiple reflections of solar

radiation (Eq. 15) may be reformulated as:

$$\begin{aligned}
W_{o,r}(\vec{y}_{i+1}, -\vec{\omega}_i, \lambda) = P_\rho \left[H(\vec{y}_{i+1} \in \partial\mathcal{D}_{S,F}^L) \int_{\Delta\Omega_d} p_{\Omega_d} d\Omega(\vec{\omega}_d) W_{o,r,d}^L(\vec{y}_{i+1}) + \right. \\
\left. \int_{2\pi} p_\rho d\Omega(\vec{\omega}_{i+1}) \left(W_{o,sky}(\vec{y}_{i+1}) + W_{o,r,d}^F(\vec{y}_{i+1}) + \right. \right. \quad (19) \\
\left. \left. + H(\vec{y}_{i+2} \in \partial\mathcal{D}_{S,F}) W_{o,r}(\vec{y}_{i+2}, -\vec{\omega}_{i+1}, \lambda) \right) \right],
\end{aligned}$$

with the following quantities corresponding to the contributions of the diffuse solar radiation from the sky (Eq. 20) and from the reflection of direct solar radiation on Lambertian (Eq. 21) or specular surfaces (Eq. 22):

$$W_{o,sky}(\vec{y}_i) = \varepsilon(\vec{y}_0) \pi H(\vec{y}_{i+1} \in \partial\mathcal{D}_{sky}) f_{sky}(-\vec{\omega}_i) I_{o,d}(\vec{y}_i), \quad (20)$$

$$W_{o,r,d}^L(\vec{y}_i) = \varepsilon(\vec{y}_0) H(\vec{y}_d \in \partial\mathcal{D}_d) |\vec{\omega}_d \cdot \vec{n}_i| D_o(\vec{y}_i), \quad (21)$$

$$W_{o,r,d}^F(\vec{y}_i) = \varepsilon(\vec{y}_0) \pi H(\vec{y}_i \in \partial\mathcal{D}_{S,F}^F) H(\vec{y}_{i+1} \in \partial\mathcal{D}_d) I_{o,d}(\vec{y}_i), \quad (22)$$

and directional PDFs:

$$p_\rho(\vec{y}_{i+1}, -\vec{\omega}_i, -\vec{\omega}_{i+1}, \lambda) = f_\rho(\vec{y}_{i+1}, -\vec{\omega}_i | -\vec{\omega}_{i+1}, \lambda) |\vec{\omega}_{i+1} \cdot \vec{n}_{i+1}|, \quad p_\Omega(\vec{\omega}_0) = \frac{|\vec{\omega}_0 \cdot \vec{n}_0|}{\pi}.$$

The diffuse solar intensity (Eq. 15) includes a recursivity through $I_{o,r}$, which highlights the reversed multiple reflection path. The other terms represent the sources of diffuse solar radiation that occur at each reflection and at the end of the sub-path. $W_{o,r,d}^L$ stands for the additive contribution of direct solar radiation reflection on Lambertian surfaces along the diffuse solar radiative sub-path. At path end, $W_{o,sky}$ represents the diffuse sky solar radiation. When the last reflection occurs on a specular surface and the ray ends in $\Delta\Omega_d$, the term $W_{o,r,d}^F$ represents the Sun's specular reflection. It is worth mentioning that the numerical value of $W_{o,r,d}^F$ (Eq. 22) may be several orders of magnitude higher than the other quantities (i.e., Eqs. 17, 21 and 20). This can lead to convergence issues of the MCM algorithm in the presence of specular reflections of direct solar irradiation ([30]).

2.4. Monte Carlo weight for the absorbed solar irradiation

The previous paragraphs have detailed the integral formulations for the direct and diffuse solar irradiations that can be computed with a reverse MCM ray-tracing algorithm. The expression of $W_{o,k}$ (Eq. 11) that is used to estimate the absorbed solar irradiations

along the conductive-radiative random walk, can now be obtained:

$$W_{o,k} = \frac{1}{h_T} \sum_{j=1}^{n_o} \left\{ W_{o,d}(\vec{y}_j) + \left(\sum_{m=1}^{n_{r,j}} H(\vec{y}_m \in \partial\mathcal{D}_{S,F}^L) W_{o,r,d}^L(\vec{y}_m) \right) + W_{o,sky}(\vec{y}_{n_{r,j}+1}) + W_{o,r,d}^F(\vec{y}_{n_{r,j}+1}) \right\}. \quad (23)$$

n_o is the number of RBC reached where a realization of the absorbed solar irradiation should be computed. $n_{r,j}$ is the number of reflections along a diffuse solar radiation sub-path. Thus, the MCM algorithm for the k th realization consists in recording the n_o direct and diffuse solar contributions. The diffuse contribution is obtained by adding $n_{r,j}$ potential reflections of the direct solar radiation, and if the sub-path ends either in the sky or as a specular reflection of the Sun, their contributions are added.

As for the computation time, it is determined by the number of realizations, which can be large for image generation. However, the independence between MCM realizations allows efficient parallelization of the algorithm. The observed computation time of the MCM algorithm (programmed with the star-engine libraries [32]) is between 100 and 1000 microseconds per realization on a single thread of a CPU (Intel® Core™ i9-9900K CPU @ 3.60GHz \times 16). This time depends on the type and the number of sub-paths computed during each realization. It also depends on the distance (in space or time) between the probe point and the boundary conditions or the initial condition where the paths end. After the HTM model presentation and the description of the probability method and MCM algorithms, the next sections are devoted to numerical validation of the developed model and its implementation for a heat wave scenario in a complex urban geometry.

3. Numerical validation

The conductive and radiative parts of the probabilistic model will be numerically validated in this section. Conduction is solved with the backward MCM algorithm in three cases of increasing geometrical complexity: 1) Case 1 considers a one-dimensional slab with a single homogeneous layer; 2) Case 2 considers a one-dimensional slab with two homogeneous layers in thermal contact; 3) Case 3 considers a three-dimensional thermal-bridge imitating a thermal bridge at a building edge. In all cases, the physical properties of each material are assumed constant, homogeneous and isotropic. To validate numerically the model, materials close to the urban context are chosen. Concrete represents the building structure and the expanded polystyrene (EPS) is chosen as a representative material for thermal insulation (Tab. 1). In addition, the solar and thermal radiation heat transfers are not accounted for in these first three cases. To quantify the accuracy of MCM, deterministic methods are used to compute temperatures ($T_{s,ref}$) that are considered as reference

results. For this purpose, the finite difference method (FDM) is used to compute the reference results in the one-dimensional cases 1, 2 and 3, while the finite volume method is used in the three-dimensional case 4. Thus, a scaled difference, ΔE_{MC} (%), between the temperatures computed with the deterministic methods and MCM are defined:

$$\Delta E_{MCM} = 100 \frac{T_{s,ref} - \tilde{T}_s}{T_{max} - T_{min}}, \quad (24)$$

where the scaling of the temperature difference is made with the maximum temperature difference occurring in the thermal problem (T_{max} is the maximum temperature and T_{min} is the minimum temperature).

In Case 1, the thermal quenching of the slab is studied numerically by confronting the reference results of FDM and the presented backward MCM algorithm based on the probabilized heat transfer model. The transient thermal problem of Case 1 includes Eqs. 1a, 1b and 1e. Table 2 gathers the initial, boundary and simulation parameters. Both slab boundaries have the same fluid temperature: $T_F(x = 0) = T_{F,i} = T_F(x = L) = T_{F,e}$ (with L the thickness of the slab). The temperature profiles at several times are plotted for a concrete slab of thickness 0.2 m in Fig. 3a and for an EPS slab of thickness 0.1 m in Fig. 3b. A uniform discretization of space and time was adopted in the FDM computation with a spatial step Δx and a time step Δt given in Tab. 2. The number of MCM realizations N with the boundary reinjection length δ_b and the absorbing thickness ϵ_b are also given in Tab. 2. Temperature profiles of Figs 3a and 3b with their scaled differences, Figs. 3c and 3d, show very good agreement between the FDM and MCM results for all locations and times considered. The FDM results are within the MCM confidence interval of $\pm 3 \tilde{\sigma}_{\tilde{T}_s}$ (corresponding to a confidence interval of 99.73 %). As expected, EPS is cooling faster than the concrete due to its lower thermal inertia (see Tab. 1).

In Case 2, a slab with two layers is considered: The first layer is constituted of EPS with thickness 0.1 m, and the second layer is constituted of concrete with thickness 0.2 m. At τ_I , both layers are at T_I (see Tab. 2) and then they are considered to exchange heat with two fluids at different temperatures: $T_F(x = 0) = T_{F,i}$ and $T_F(x = L) = T_{F,e}$ (with L the overall thickness of the slab, i.e., 0.3 m). Both sides have identical convective heat transfer coefficients. The thermal problem of Case 2 includes Eqs. 1a, 1b, 1e and 1d. Resulting temperature profiles inside the two-layer slab are shown at four different times in Figs. 3e-3f and the simulation parameters for the FDM and MCM simulations are gathered in Tab. 2. Figures 3e-3f show very good agreement between the FDM and MCM results. In addition, the FDM results are within the MCM confidence interval. Soon after the initial time, EPS exhibits the largest temperature difference due to its low conductivity and low thermal inertia. Concrete is heating up slowly but more uniformly than EPS due to its higher thermal inertia and conductivity. The thermal problem of Case 3 is identical to case

2 but its geometry and temperature field are more complex. Geometry of Case 3 is depicted in Fig. 4 with two views, along $+Y$ and $-Z$ axis, showing the location of concrete and EPS in a typical building thermal bridge configuration. Considering the symmetry of this domain, Case 3 represents stacked cubic rooms with an edge of 2.4 m where the floors and the lateral envelope are in concrete (0.2 m thickness). In each room, an internal insulation is considered with a vertical EPS layer of 0.1 m thickness. The thermal simulation consists in heating the solids by convection from the external concrete envelope, while the room internal fluid is set at the initial temperature. To produce the reference solution, a finite-volume method (FVM) was chosen. The application `chtMultiRegionFoam` of OpenFoam v9 was used to solve Case 3 with a preconditioned bi-conjugate gradient solver and a Gauss linear corrected scheme (second order) for the Laplacian discretization. The unstructured three-dimensional hexahedra mesh was generated with the `snappyHexMesh` utility from triangulated surface geometry. A characteristic spatial step of the mesh is given in Tab. 2 but a refined zone was set to halve this characteristic step that is defined as a box with two points: $[0.2; 0.2; 0]$ and $[0.6; 0.6; 0.3]$. This refined zone is best seen in Fig. 4c where the temperature field is drawn in plane $X = 0.25$ at time $t = 8 \times 10^4$ in the thermal bridge zone. The exterior fluid temperature being higher than the interior one, heat is conducted preferentially in the concrete floor. A numerical comparison is plotted in Fig. 5a where the whole transient temperature field is computed with OpenFoam (e.g., Fig. 4c) whereas the MCM was used to compute solid temperatures at three locations and several times: Two computation points are located inside the solids in the thermal bridge corner, one in EPS with coordinates $[0.35; 0.35; 0.15]$ and one in concrete with coordinates $[0.5; 0.5; 0.05]$; A third point is located on the external concrete wall with coordinates $[0.6; 0.5; 0.05]$. The lower transient temperatures are computed at the point inside the insulation, while the higher transient temperatures in Fig. 5a are computed for the point on the external wall. The plot of the scaled differences between FVM and MCM in Fig. 5b highlights a weak trend associated to the temperatures computed by MCM to be slightly higher than the one computed by FVM. The values of ΔE_{MCM} being lower than 1.5 % of the observed discrepancies may be considered acceptable and potentially attributed to the numerical diffusion associated to FVM and/or the numerical implementation of WOS with the parameters δ_b and ϵ_b .

The three cases have demonstrated the ability of the proposed probabilistic model and algorithm to solve conductive heat transfer with probabilized RBC in complex geometry. Thus, the accuracy of the radiative part of the proposed model will be studied numerically in the following Case 4. This will be done through a comparison with reference results obtained by a MCM model validated in [30] and implemented in the HTRDR-Urban code [33]. A urban scene is selected for the validation and the objective is to compare the (instantaneous) infrared thermal renderings that involve only the radiative exchanges be-

cause all the temperatures are set. A CIE tristimulus [34] rendering of the urban geometry is shown in Fig. 5c. The geometry includes a flat ground and two parallel rows, separated by 15 m, of five buildings with 5 m spacings. The building heights are set to 16.7 m (5 floors), their lengths to 11.5 m and their widths to 7 m. All surfaces are assumed opaque. The ground and the building walls are Lambertian, but the windows are specular. Their temperatures and gray optical properties are gathered in Tab. 2. The 300x300 pixels image of the infrared rendering computed by HTRDR-Urban is plotted in Fig. 5d. The temperature of each pixel is a radiance temperature (or equivalent black body temperature) with $N = 10^3$ sample per pixel. Its value takes into account the multiple reflections driven by the surface optical properties (Tab. 2) that are all at the same temperature, except the sky. The low radiance temperatures of the ground are due to its low emissivity and the low temperature of the sky. Between the buildings, pixel radiance temperatures present high values due to the multiple reflections. In addition, specular surfaces present high radiance temperatures because their normal emissivity is high. The proposed model gives similar results which are not shown for the sake of conciseness. Instead, the pixel-based scaled differences are plotted in Fig. 5e. Absolute values of ΔE_{MCM} are lower than 3%, and their repartition in the image (Fig. 5e) highlights its origin comes from the statistical noise associated with each MCM computation (HTRDR-Urban and the present model). In this section, the random walks used to solve radiative and conductive heat transfers along with the probabilization at the interfaces (Robin's and solid-solid boundary conditions) were validated. In the next section, the proposed model is applied to a complex urban geometry for heat wave meteorological conditions.

4. Results for a heat wave conditions

The ability of the probabilistic model to solve for coupled conduction and radiation (linearized thermal and solar) in complex geometry will be used to obtain key quantities needed to study urban environments.

4.1. Geometry and simulation settings

Heat wave meteorological conditions are investigated with a geometry of aligned buildings (mimicking a street oriented East-West, Fig. 6) and trees. This choice is purely arbitrary and more advanced city geometry or higher frequency weather data could be considered. The aligned buildings are identical to those used for the validation of the radiative model (i.e., Figs. 5c-5d), but their number is doubled to reach two rows of ten aligned buildings (Fig. 6a). The concrete building walls, the glass windows and the ground have homogeneous and isotropic thermal properties gathered in Tab. 1. The buildings and a surface body (Fig. 6a) were created for the scenario. The tree geometry was obtained from

a study conducted with DART (Discrete Anisotropic Radiative Transfer model) in project RAMI-V (RAdiation transfer Model Intercomparison V) [35]. Trees are aligned along the street centre, and the trunks are separated by 8.5 m. Each 12 m high tree is made of a trunk (4 m high) topped with a spherical foliage of 8 m in diameter, centred at 8 m above the ground. The foliage is made of numerous small triangular surfaces representing an average specific surface of 0.021 m^{-1} . The time evolution of solar irradiations (direct and diffuse) are plotted in Fig. 6b for the five days heat wave scenario with the external air temperatures given by the formula:

$$T_{F,e}(t) = 308.15 + 5 \sin(2\pi[t - 0.4]), \quad (25)$$

where the units of time t is days. Each MCM simulation is computed at an observation time relatively to the initial time $\tau_I = 0$ (see Fig. 6b) which is considered to be the 21st of June 2016 at midnight. This date, the latitude (43.479) and longitude (-1.509) are used to compute the Sun's direction. The transient sky model for solar radiation assumes a clear sky with an isotropic diffuse irradiation. $H_{o,sky}$ (Fig. 6b) is the diffuse solar irradiation on an horizontal surface. The direct solar radiation (D_o in Fig. 6b) is emitted by the Sun's disk with half angle θ_d . Its value and MCM simulation parameters are gathered in Tab. 2. The transient sky model for thermal radiation considers the sky as a black body with uniform temperature T_{sky} (see Tab. 2). In this scenario, at the initial time, all the solids are at T_I . During the transient simulation, two Dirichlet's boundary conditions (Eq. 1c) are set: T_g , for the ground at its thickness depth; and T_b , the body surface (Fig. 6a) temperature. RBC are applied to the surfaces adjacent to external or internal air such as the ground, the building walls and the window glasses. The room air temperatures in each building are set identical and equal to $T_{F,i}$. Temperatures involved in the heat wave scenario simulations are gathered in Tab. 2.

4.2. Mean radiant temperature and energy consumption

The key quantities to compute are the mean radiant temperature (MRT) and energy consumption. MRT is related to the outdoor comfort by various indicators. It defines an equivalent temperature for the environment of a body surface (S_b), and its expression is:

$$\bar{T}_{R,b}(t) = \left[\frac{1}{\sigma_{SB} S_b} \int_{S_b} dA(\vec{y}_0) H_b(\vec{y}_0, t) \right]^{\frac{1}{4}}, \quad (26)$$

where the body surface considered is depicted in Fig. 6a and the total irradiation (from thermal and solar radiation) is given by:

$$H_b(\vec{y}_0, t) = \int_0^{+\infty} d\lambda \int_{2\pi} d\Omega(\vec{\omega}_0) |\vec{\omega}_0 \cdot \vec{n}_0| I(\vec{y}_0, t, -\vec{\omega}_0, \lambda).$$

Figure 6 shows Mollweide projections onto a disc of the thermal environment around the body surface with and without the trees. This rendering is obtained by computing θ_R with MCM for each pixel (image with resolution 300x300) with $N = 10^3$, at 1 pm the first day of the heat wave scenario. This small number of realizations leads to $\sigma_{\tilde{T}_R} \leq 0.4$ K for the pixels of buildings, and $\sigma_{\tilde{T}_R} \leq 0.8$ K for the pixels of the ground. The south being in the middle of the right part of the disc, one can observe the effects of solar shading on the ground temperatures caused by the buildings and the trees (Fig. 6c). In addition, south facing building facades present higher radiance temperatures than north facing walls due to solar irradiation. It is worth recalling the computed temperatures (θ_R) are not the actual material temperatures but the radiance temperatures. Figure 7a presents the time evolution of MRT averaged on the body surface, i.e. $\tilde{T}_{R,b}$, in the street configuration during the heat wave scenario and computed by MCM for each hour. The results are given with their error bars ($\pm 3 \sigma_{\tilde{T}_{R,b}}$) corresponding to confidence intervals greater than 99.7 %. It is shown that the trees produce a reduction of the MRT maximum values during the hottest hours, but also limit nighttime radiative cooling. Indeed, the trees lead to a lower rate of daytime ground temperature increase by blocking solar radiation, but also reduce radiative cooling towards the sky at night.

To obtain the energy consumption in this heat wave scenario, the air conditioning system should be simulated. But, in this demonstration study, only the average internal wall temperature ($\bar{T}_{s,i}$) is computed. Indeed, considering an air conditioning system that maintains constant the internal air temperature ($T_{F,i}$, see Tab. 2), the energy consumption may be computed by an expression similar to Eq. 2 that requires,

$$\bar{T}_{s,i}(t) = \frac{1}{S_i} \int_{S_i} dA(\vec{y}_0) T_s(\vec{y}_0, t), \quad (27)$$

and the convective heat transfer coefficient (Tab. 2) which is set constant. The computation of $\bar{T}_{s,i}$ accounts for the solar irradiation coming through the windows. It is worth mentioning this quantity could also be of interest for indoor thermal comfort studies. Figure 7b presents hourly MCM computations of $\tilde{T}_{s,i}$ accounting for the solar gains through the windows or neglecting them (as if the shades were shut). When the solar gains are computed, some error bars are very large. This is due to some realizations of the MCM weight (Eq. 11) that are several orders of magnitude greater than the expected result. This

could be avoided by increasing the number of realizations ([30]). Indeed, in this case, it is due to rare events corresponding to a reflection of the direct Sun's radiation by a specular material (glass) during the computation of the diffuse solar irradiation (Eq. 22). Thus, it involves a MCM weight proportional to the direct radiative solar intensity which is about five orders of magnitude greater than D_o . During the first day, the buildings are cooling down because the initial temperature was set to a high value (Tab. 2). After this period driven by the thermal inertia of the buildings, a periodic behaviour of $\overline{T}_{s,i}$ may be recognized. When the solar gains are considered, the temporal variations of internal wall temperature are driven by the temporal variations of the solar heat gains. Without the internal solar gains, a small periodicity is observed corresponding to the daily weather variation smoothed and shifted by the building thermal inertia.

5. Conclusion and future work

A probabilistic thermal model is presented that solves with MCM linear and transient heat transfers by conduction and thermal radiation with RBC accounting for convection and absorption of solar radiation in urban geometry. DRT is demonstrated suitable to compute unknown direct and diffuse solar irradiations in complex urban geometry with Lambertian and specular walls. Indeed, the methodology is validated for conduction and radiation heat transfers separately in three-dimensional urban morphologies. In addition, the developed probabilistic method is applied to compute the influence of trees on MRT in a street lined by buildings for heat wave meteorological conditions. The impact of solar gains on the indoor wall temperatures is also quantified. Trees decrease MRT during daytime with solar shadowing, but increase MRT during nighttime with their leaves limiting the radiative cooling with the clear sky. Indoor solar gains increase the average wall temperatures and the cooling effort during daytime. The influence of rare specular reflections of direct solar radiation on MCM results has been documented.

Future work includes improvements to the current model and applications to real cities. Some improvements to this model could include the development of a model for the air temperatures inside the building, the addition of radiation in semi-transparent media and conduction with volumetric heat sources, and the consideration of non-linear radiative exchange between surfaces. Application to real cities may also involve sensitivity studies to parameters and the development of fast and accurate methods to efficiently couple this probabilistic heat transfer model with urban microclimate fluid flow simulations.

Acknowledgments

Funding: This work was partly supported by the French National Research Agency (MC2 ANR-21-CE46-0013) and the E2S UPPA initiatives.

References

- [1] K. G. Burkart, M. Brauer, A. Y. Aravkin, W. W. Godwin, S. I. Hay, J. He, V. C. Iannucci, S. L. Larson, S. S. Lim, J. Liu, C. J. L. Murray, P. Zheng, M. Zhou, J. D. Stanaway, Estimating the cause-specific relative risks of non-optimal temperature on daily mortality: a two-part modelling approach applied to the Global Burden of Disease Study, *The Lancet* 398 (10301) (2021) 685–697, publisher: Elsevier. doi : 10.1016/S0140-6736(21)01700-1.
- [2] C. Li, J. Zhou, Y. Cao, J. Zhong, Y. Liu, C. Kang, Y. Tan, Interaction between urban microclimate and electric air-conditioning energy consumption during high temperature season, *Applied Energy* 117 (2014) 149–156. doi:https://doi.org/10.1016/j.apenergy.2013.11.057.
- [3] B. Blocken, Computational fluid dynamics for urban physics: Importance, scales, possibilities, limitations and ten tips and tricks towards accurate and reliable simulations, *Building and Environment* 91 (2015) 219–245. doi:10.1016/j.buildenv.2015.02.015.
- [4] A. J. Arnfield, Two decades of urban climate research: a review of turbulence, exchanges of energy and water, and the urban heat island, *International Journal of Climatology* 23 (1) (2003) 1–26. doi:https://doi.org/10.1002/joc.859.
- [5] N. Villefranque, F. Hourdin, L. d’Alençon, S. Blanco, O. Boucher, C. Caliot, C. Coustet, J. Dauchet, M. E. Hafi, V. Eymet, O. Farges, V. Forest, R. Fournier, J. Gautrais, V. Masson, B. Piaud, R. Schoetter, The ”teapot in a city”: A paradigm shift in urban climate modeling, *Science Advances* 8 (27) (2022) eabp8934. doi : 10.1126/sciadv.abp8934.
- [6] C. S. B. Grimmond, M. Blackett, M. J. Best, J. Barlow, J.-J. Baik, S. E. Belcher, S. I. Bohnenstengel, I. Calmet, F. Chen, A. Dandou, K. Fortuniak, M. L. Gouvea, R. Hamdi, M. Hendry, T. Kawai, Y. Kawamoto, H. Kondo, E. S. Krayenhoff, S.-H. Lee, T. Loridan, A. Martilli, V. Masson, S. Miao, K. Oleson, G. Pigeon, A. Porson, Y.-H. Ryu, F. Salamanca, L. Shashua-Bar, G.-J. Steeneveld, M. Tombrou, J. Voogt, D. Young, N. Zhang, The International Urban Energy Balance Models Comparison Project: First Results from Phase 1, *Journal of Applied Meteorology and Climatology* 49 (6) (2010) 1268–1292. doi : 10.1175/2010JAMC2354.1.
- [7] V. Masson, A Physically-Based Scheme For The Urban Energy Budget In Atmospheric Models, *Boundary-Layer Meteorology* 94 (3) (2000) 357–397. doi : 10.1023/A:1002463829265.

- [8] K. W. Oleson, G. B. Bonan, J. Feddema, M. Vertenstein, C. S. B. Grimmond, An Urban Parameterization for a Global Climate Model. Part I: Formulation and Evaluation for Two Cities, *Journal of Applied Meteorology and Climatology* 47 (4) (2008) 1038–1060. doi:10.1175/2007JAMC1597.1.
- [9] J. Bouyer, C. Inard, M. Musy, Microclimatic coupling as a solution to improve building energy simulation in an urban context, *Energy and Buildings* 43 (7) (2011) 1549–1559. doi:10.1016/j.enbuild.2011.02.010.
- [10] Y. Toparlar, B. Blocken, B. Maiheu, G. J. F. v. Heijst, A review on the CFD analysis of urban microclimate, *Renewable and Sustainable Energy Reviews* 80 (2017) 1613–1640. doi:https://doi.org/10.1016/j.rser.2017.05.248.
- [11] H. Ge, V. R. McClung, S. Zhang, Impact of balcony thermal bridges on the overall thermal performance of multi-unit residential buildings: A case study, *Energy and Buildings* 60 (2013) 163–173. doi:10.1016/j.enbuild.2013.01.004.
- [12] J. del Coz Díaz, P. García Nieto, C. Betegón Biempica, M. Prendes Gero, Analysis and optimization of the heat-insulating light concrete hollow brick walls design by the finite element method, *Applied Thermal Engineering* 27 (8-9) (2007) 1445–1456. doi:10.1016/j.applthermaleng.2006.10.010.
- [13] J. Delatorre, G. Baud, J. J. Bézian, S. Blanco, C. Caliot, J. F. Cornet, C. Coustet, J. Dauchet, M. El Hafi, V. Eymet, R. Fournier, J. Gautrais, O. Gourmel, D. Joseph, N. Meilhac, A. Pajot, M. Paulin, P. Perez, B. Piaud, M. Roger, J. Rolland, F. Veynandt, S. Weitz, Monte Carlo advances and concentrated solar applications, *Solar Energy* 103 (2014) 653–681. doi:10.1016/j.solener.2013.02.035.
- [14] R. Fournier, S. Blanco, V. Eymet, M. E. Hafi, C. Spiesser, Radiative, conductive and convective heat-transfers in a single Monte Carlo algorithm, Vol. 676, 2016, p. 012007. doi:10.1088/1742-6596/676/1/012007.
- [15] C. Caliot, S. Blanco, C. Coustet, M. E. Hafi, V. Eymet, R. Fournier, B. Piaud, Combined conductive-radiative heat transfer analysis in complex geometry using the monte carlo method, in: *CTRPM-VI - 6th Computational Thermal Radiation in Participating Media*, 2018, p. 9.
- [16] L. Ibarrart, C. Caliot, M. El Hafi, R. Fournier, S. Blanco, S. Dutour, J. Dauchet, J.-M. Tregan, V. Eymet, V. Forest, Combined conductive-convective-radiative heat transfer in complex geometry using the Monte Carlo method: Application to solar receivers, in: *International Heat Transfer Conference*, Vol. 2018-August, 2018, pp. 8135–8142,

cited By :4.

URL www.scopus.com

- [17] M. Sans, O. Farges, V. Schick, C. Moyne, G. Parent, Modeling the Flash method by using a conducto-radiative Monte Carlo algorithm: Application to porous media, in: *Proceeding of Proceedings of the 9th International Symposium on Radiative Transfer, RAD-19*, Begellhouse, Athens, Greece, 2019, pp. 319–326. doi : 10.1615/RAD-19.390.
- [18] G. A. Mikhailov, Randomized Monte Carlo Algorithms for Problems with Random Parameters (“Double Randomization” Method), *Numerical Analysis and Applications* 12 (2) (2019) 155–165. doi : 10.1134/S1995423919020058.
- [19] J.-M. Tregan, J.-L. Amestoy, M. Bati, J.-J. Bézian, S. Blanco, L. Brunel, C. Caliot, J. Charon, J.-F. Cornet, C. Coustet, L. D’alençon, J. Dauchet, S. Dutour, S. Eibner, M. El-Hafi, V. Eymet, O. Farges, V. Forest, R. Fournier, M. Galtier, V. Gattepaille, J. Gautrais, Z. He, F. Hourdin, L. Ibarart, J.-L. Joly, P. Lapeyre, P. Lavieille, M.-H. Lecureux, J. Lluc, M. Miscovic, N. C. Mourtaday, Y. NYFFENEGGER-PERE, L. P. Pelissier, L. Penazzi, B. Piaud, C. Rodrigues-Viguier, G. Roques, M. Roger, T. Saez, G. Terrée, N. Villefranque, T. Vourc’h, D. Yaacoub, Coupling radiative, conductive and convective heat-transfers in a single Monte Carlo algorithm: a general theoretical framework for linear situations, working paper or preprint (Oct. 2022).
- [20] L. Ibarart, S. Blanco, C. Caliot, J. Dauchet, S. Eibner, M. El-Hafi, O. Farges, V. Forest, R. Fournier, J. Gautrais, R. Konduru, L. Penazzi, J.-M. Tregan, T. Vourc’h, D. Yaacoub, Advection, diffusion and linear transport in a single path-sampling Monte-Carlo algorithm : getting insensitive to geometrical refinement, working paper or preprint (Oct. 2022).
- [21] J. Novák, I. Georgiev, J. Hanika, W. Jarosz, Monte Carlo Methods for Volumetric Light Transport Simulation, *Computer Graphics Forum* 37 (2) (2018) 551–576. doi : 10.1111/cgf.13383.
- [22] I. Wald, S. Woop, C. Benthin, G. S. Johnson, M. Ernst, Embree: a kernel framework for efficient CPU ray tracing, *ACM Transactions on Graphics* 33 (4) (2014) 1–8. doi : 10.1145/2601097.2601199.
- [23] L. Penazzi, S. Blanco, C. Caliot, C. Coustet, M. El-Hafi, R. Fournier, J. Gautrais, M. Sans, A. Golijanek-Jedrzyjczyk, Path integrals formulations leading to propagator evaluation for coupled linear physics in large geometric models, working paper or preprint (Nov. 2022).

- [24] H. Janssen, B. Blocken, J. Carmeliet, Conservative modelling of the moisture and heat transfer in building components under atmospheric excitation, *International Journal of Heat and Mass Transfer* 50 (5-6) (2007) 1128–1140. doi:10.1016/j.ijheatmasstransfer.2006.06.048.
- [25] M. Bati, S. Blanco, C. Coustet, V. Eymet, V. Forest, R. Fournier, J. Gautrais, N. Mellado, M. Paulin, B. Piaud, Coupling conduction, convection and radiative transfer in a single path-space: Application to infrared rendering, in: *ACM Transactions on Graphics (Proceedings of SIGGRAPH)*, Vol. 42, pp. 1–20. arXiv:hal-04090428v2, doi:10.1145/3592121.
- [26] J. K. Salmon, M. A. Moraes, R. O. Dror, D. E. Shaw, Parallel random numbers: As easy as 1, 2, 3, in: *Proceedings of 2011 International Conference for High Performance Computing, Networking, Storage and Analysis, SC '11*, Association for Computing Machinery, New York, NY, USA, 2011. doi:10.1145/2063384.2063405.
- [27] A. Haji-Sheikh, E. M. Sparrow, The Floating Random Walk and Its Application to Monte Carlo Solutions of Heat Equations, *SIAM Journal on Applied Mathematics* 14 (2) (1966) 370–389. doi:10.1137/0114031.
- [28] K. K. Sabelfeld, A global random walk on spheres algorithm for transient heat equation and some extensions, *Monte Carlo Methods and Applications* 25 (1) (2019) 85–96. doi:10.1515/mcma-2019-2032.
- [29] N. Villefranque, R. Fournier, F. Couvreur, S. Blanco, C. Cornet, V. Eymet, V. Forest, J.-M. Tregan, A path-tracing Monte Carlo library for 3-D radiative transfer in highly resolved cloudy atmospheres, *J Adv Model Earth Syst* 11 (8) (2019) 2449–2473. doi:10.1029/2018MS001602.
- [30] C. Caliot, R. Schoetter, V. Forest, V. Eymet, T.-Y. Chung, Model of Spectral and Directional Radiative Transfer in Complex Urban Canopies with Participating Atmospheres, *Boundary-Layer Meteorology* (Oct. 2022). doi:10.1007/s10546-022-00750-5.
- [31] R. Perez, R. Seals, J. Michalsky, All-weather model for sky luminance distribution—preliminary configuration and validation, *Solar Energy* 50 (3) (1993) 235–245. doi:10.1016/0038-092X(93)90017-I.
- [32] Méso-Star, Star-engine library for Monte Carlo numerical simulations.
URL <https://gitlab.com/meso-star/star-engine>

- [33] C. Caliot, R. Schoetter, V. Forest, V. Eymet, T.-Y. Chung, Starter Pack and validation scripts for the Monte- Carlo-based urban radiative transfer model described in "Model of Spectral and Directional Radiative Transfer in Complex Urban Canopies with Participating Atmospheres", submitted to Boundary- Layer Meteorology (Mar. 2022). doi : 10.5281/zenodo.6370467.
- [34] C. Wyman, P.-P. Sloan, P. Shirley, Simple analytic approximations to the CIE XYZ color matching functions, Journal of Computer Graphics Techniques (JCGT) 2 (2) (2013) 1–11.
- [35] Radiation transfer model intercomparison RAMI V, <https://rami-benchmark.jrc.ec.europa.eu/> (2020).
URL <https://dart.omp.eu/index.php#/doc>

Nomenclature

Latin symbols

C_p	specific heat capacity
\mathcal{D}	domain
D	direct normal irradiation
d	thickness
F	Fresnel's reflectivity
f	function
h	heat transfer coefficient
$H(\cdot)$	Heaviside's test function
H	irradiation
I	radiative intensity
I_b	blackbody radiative intensity
k	thermal conductivity
\vec{n}	outward normal vector
N	number of samples
(n, k)	complex refractive index
P	probability
p	PDF
\dot{q}	heat flux
\vec{R}	specular direction
S	surface area
T	temperature
t	time
W	MCM weight
\vec{x}, \vec{y}	coordinate vectors

Greek symbols

α	thermal diffusivity
δ	Dirac's delta function
δ_b	boundary reinjection length
ΔE	scaled difference
ε	emissivity
ϵ_b	absorbing thickness
λ	wavelength

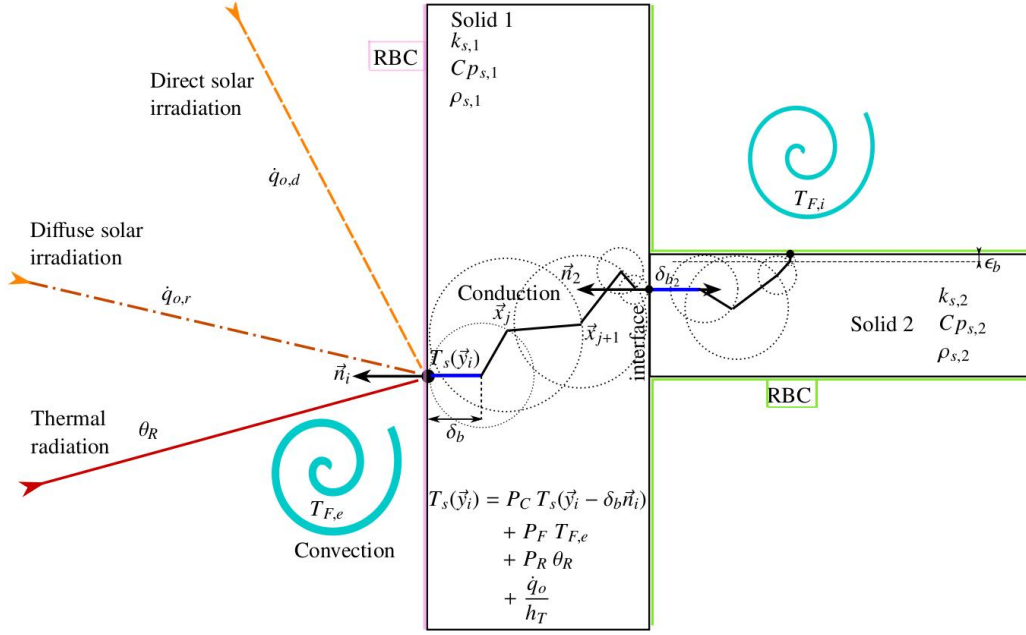
Ω	solid angle
$\vec{\omega}$	direction vector
ρ	density or reflectivity
σ	standard error
τ	time
θ_d	Sun's half angle
θ_R	radiative temperature

Superscripts

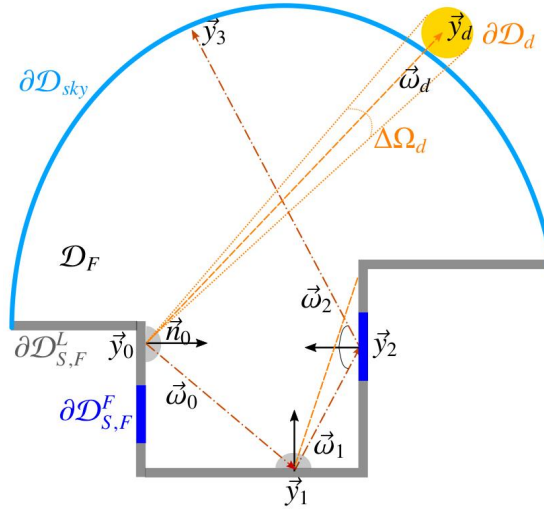
\cap	hemispherical
F	specular surface
L	Lambertian surface
'	directional

Subscripts

1, 2	indexes for solids
b	body
C	conduction
D	Dirichlet's condition
d	direct
e	external
F	fluid domain or specular surface
g	ground
I	initial condition
i	internal, or index
j, k	indexes
L	Lambertian surface
n	number of jumps
o	solar
R	radiation
r	diffuse radiation or reference radiative temperature
$^{24}S, s$	solid domain
T	total



(a) Representation of random paths starting at an outdoor wall with RBC to compute $T_s(\vec{y}_i)$



(b) Examples of solar direct and diffuse sub-paths

Figure 1: Schematic representation of conductive, thermal and solar radiative sub-paths: (a) Sub-path realizations for direct and diffuse solar irradiances, absorbed at \vec{y}_i , are drawn. A path starting at \vec{y}_i is chosen randomly among conductive, convective and radiative heat transfer modes (Eq. 10). A floating WOS is depicted. When crossing the interface between solid 1 and 2, a position in the solid 2 is randomly chosen and the path terminates at an indoor RBC where the room air temperature is retained ($T_{F,i}$); (b) The sky (\mathcal{D}_{sky}) and the urban geometry ($\mathcal{D}_{S,F}$) form an enclosure filled with a transparent medium where radiation is multiply reflected. The Sun's surface (\mathcal{D}_d), Lambertian and specular reflecting materials are also represented. A realization of $\dot{q}_{o,d}(\vec{y}_0)$ is drawn with a realization of $\dot{q}_{o,r}(\vec{y}_0)$ that includes a shadowed direct contribution at \vec{y}_1 , a specular reflection at \vec{y}_2 and a path ending in the sky

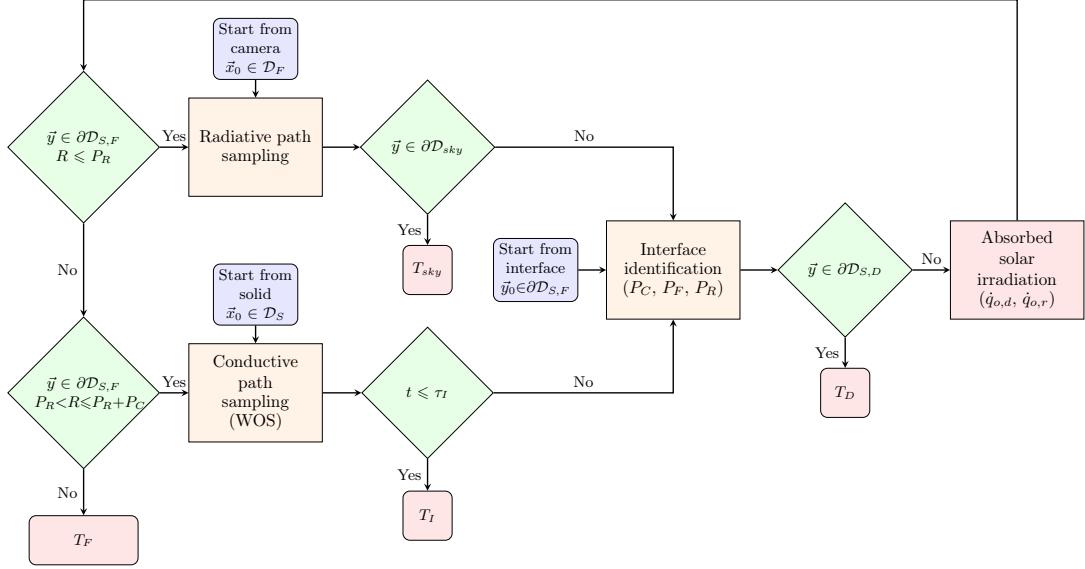


Figure 2: Flowchart of the backward MCM algorithm used to compute one realization of a MCM temperature estimate in an urban geometry. Three starting locations are given in blue rounded squares: inside the solid, or inside the fluid (camera), or at an interface. Four temperatures at path ends are given in red rounded squares: initial, sky, fluid or Dirichlet’s boundary temperatures. Green diamonds specify a condition with two outcomes (Yes/No). Orange rectangles stand for specific algorithms, which generate radiative or conductive paths, or identify the reached interfaces where the double randomization may occur. The red rectangle represents the evaluation of solar contributions

Table 1: Thermal properties of materials with their thickness (d) and their reflectivity (solar and thermal) or their refractive index (with real and imaginary parts) used in the numerical validation cases (1-3) and for the heat wave scenario

Material	λ_s (W m ⁻¹ K ⁻¹)	ρ_s (kg m ⁻³)	$C_{p,s}$ (J kg ⁻¹ K ⁻¹)	d (m)	P_{ρ_o} or (n, k)	P_{ρ_R} or (n, k)
concrete	1.8	2400	1000	0.4	0.8	0.2
EPS	0.035	20	1300	–	–	–
ground	1	1300	1900	10	0.5	0.2
glass	1	2500	900	0.005	(1.52, 0)	(1.7, 0.636)
body	–	–	–	–	0	0
tree	–	–	–	–	0.2	0

Table 2: Temperatures and numerical parameters for the four validation cases and the heat wave scenario

	T_I (K)	$T_{F,i}$ (K)	$T_{F,e}$ (K)	h_F (W m ⁻² K ⁻¹)	Δx (mm)	Δt (s)	N (-)	δ_b (mm)	ϵ_b (mm)
Case 1	293.15	273.15	273.15	10	1	0.72	10 ⁵	Δx	$\delta_b/4$
Case 2	283.15	273.15	293.15	10	1	0.72	10 ⁵	Δx	$\delta_b/4$
Case 3	293.15	293.15	313.15	10	10	2	10 ⁵	$\Delta x/7$	$\delta_b/4$
		T (K)	P_ρ	(n, k)					
Case 4	ground	283.15	0.5	–					
	walls	283.15	0.5	–					
	windows	283.15	–	(1.7, 0.636)					
	sky	273.15	0	–					
	T_I	T_r	$T_{F,i}$	T_g	T_b	$T_{F,e}$	T_{sky}		
heat	305.211	298.15	298.15	283.15	300.15	Eq. 25	$T_{F,e} - 20$		
	S_i (m ²)	S_b (m ²)	h_F (W m ⁻² K ⁻¹)	θ_d (rd)	N (-)	δ_b (mm)	ϵ_b (mm)		
wave scenario	33168	1.77	10	4.65×10^{-3}	10 ⁵	2	0.5		

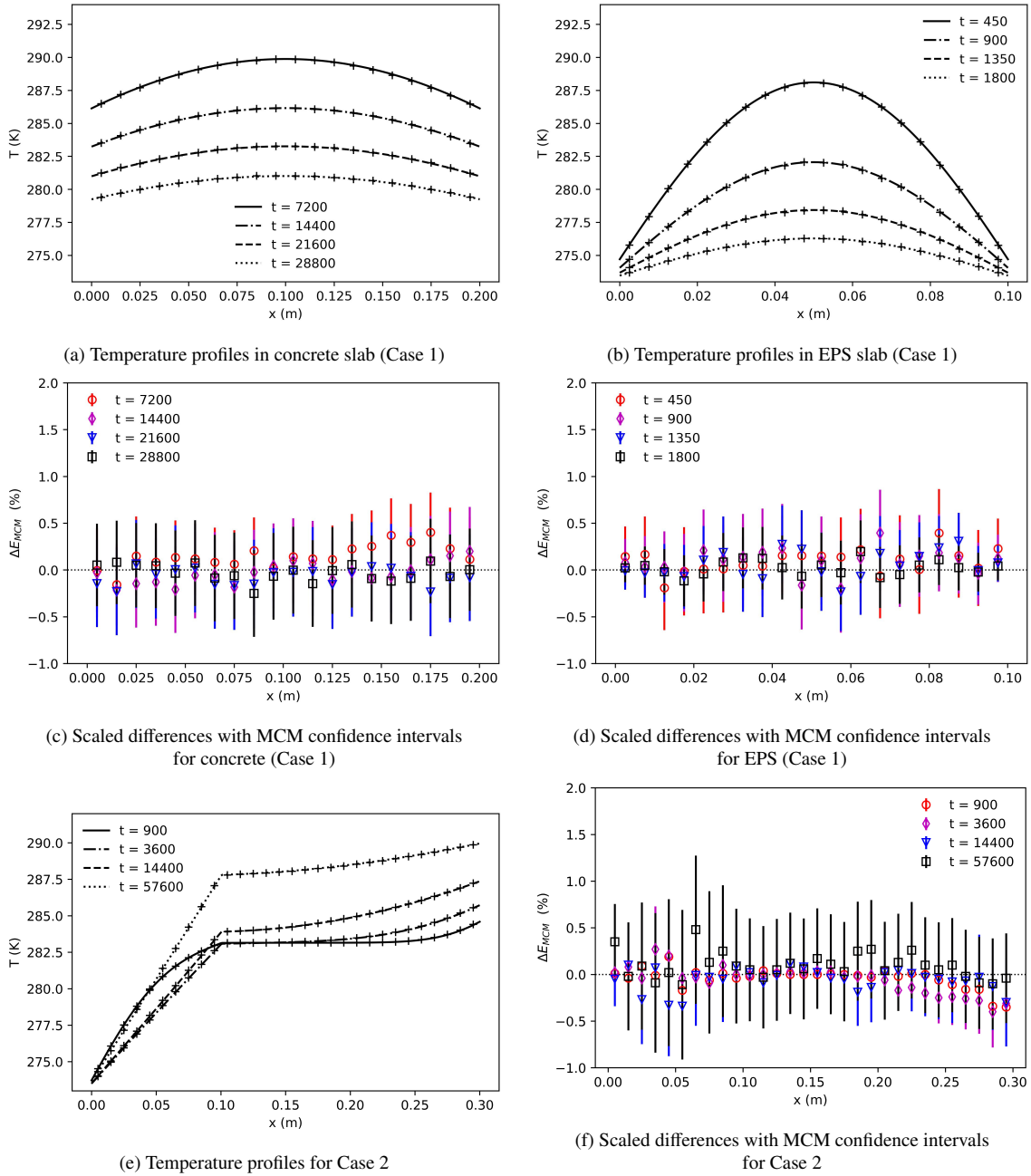


Figure 3: Comparison of temperature profiles at several times (with units s) for single-layer slabs of Case 1 (a)-(d) and the two-layer slab of Case 2 (e)-(f) obtained with the deterministic FDM (lines) and the probabilistic MCM (markers). The scaled numerical error (Eq. 24) and the MCM confidence intervals ($3\tilde{\sigma}_{T_s}$) are also given

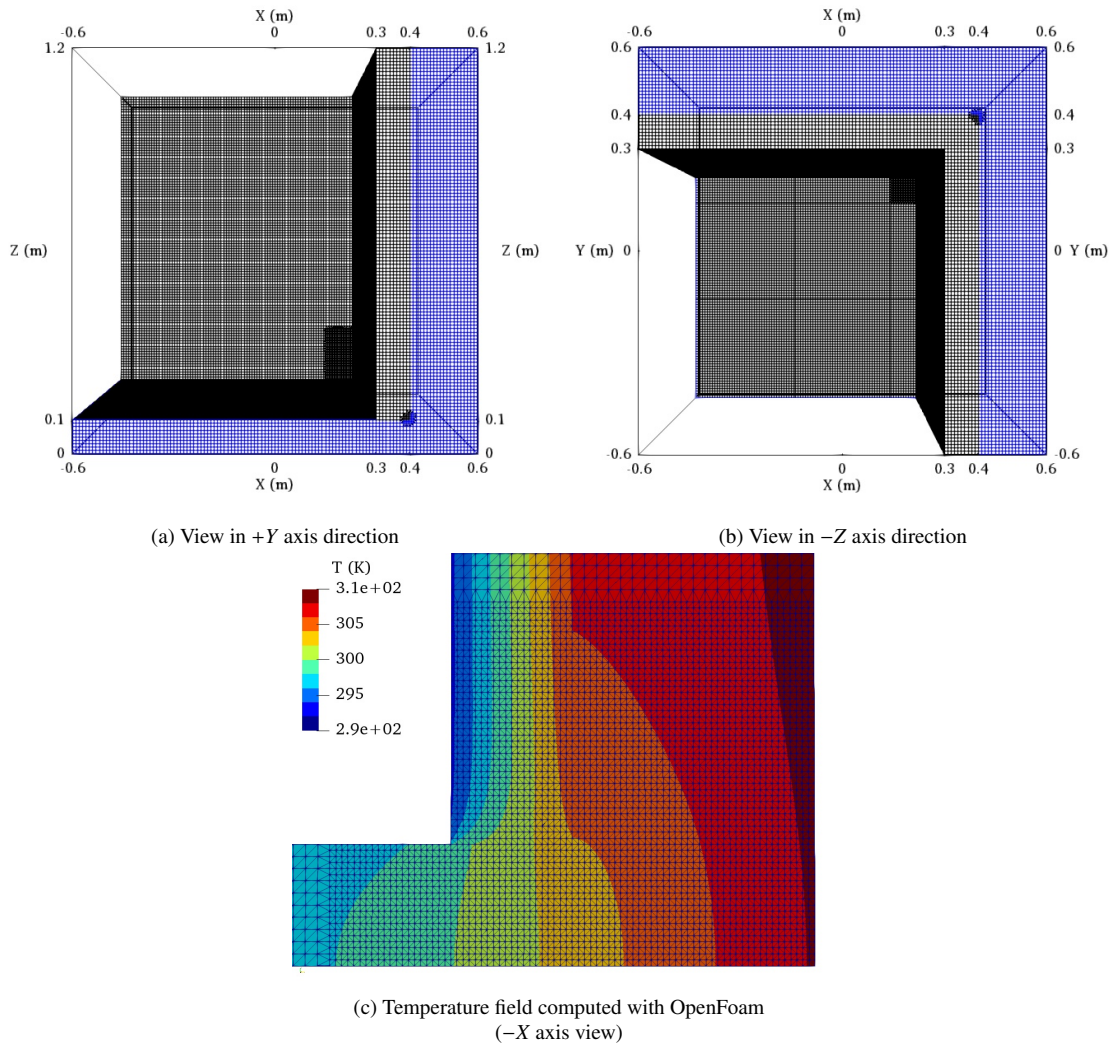


Figure 4: Geometry and computation results for Case 3: (a) View of the geometry and its mesh in the +Y axis direction, while in (b) the view is in the -Z direction. The geometry is composed of internal insulation (EPS, in black) and a structure (concrete, in blue) representing a thermal bridge in a building. The internal surfaces are the boundaries at $Z = 0.1$ m, $X = 0.3$ m, and $Y = 0.3$ m. The external surfaces are at $X = 0.6$ m, and $Y = 0.6$ m, while the symmetry boundaries are at $X = -0.6$ m, $Y = -0.6$ m, $Z = 0$ and 1.2 m. (c) The temperature field, in the plane $X = 0.25$, computed at $t = 8 \times 10^4$ s with OpenFoam is given. The external vertical boundary is located on the right while the internal vertical boundary is located on the left. The mesh is superimposed showing the refined zone inside the thermal bridge corner

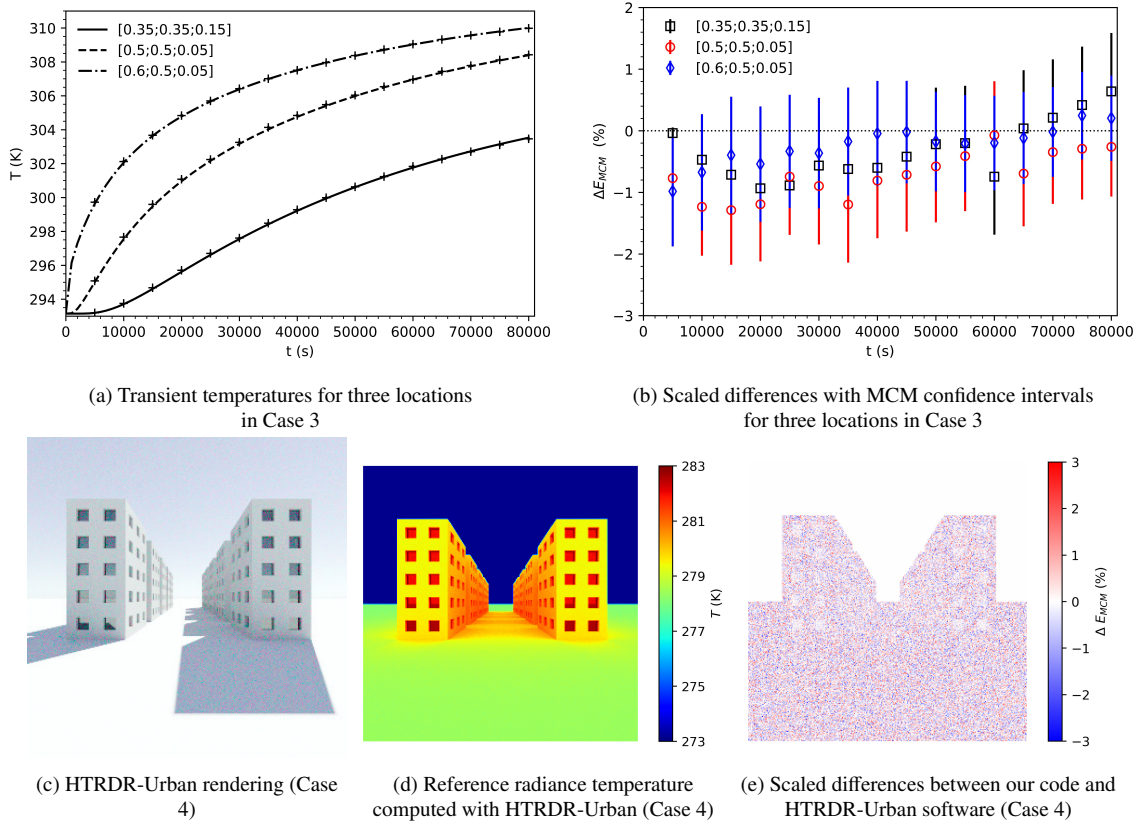
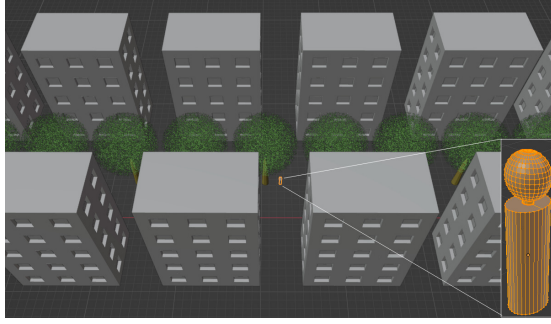
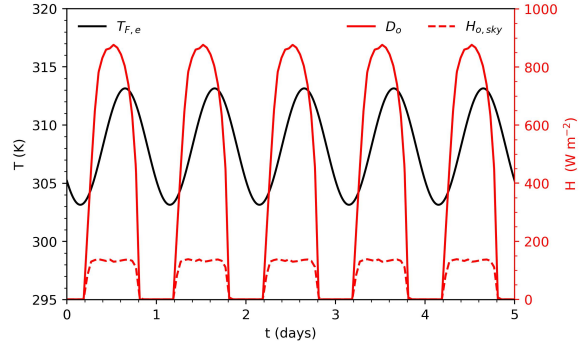


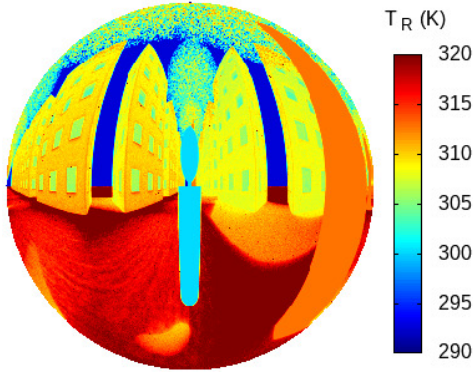
Figure 5: Numerical validation results of cases 3 and 4: Comparison of transient temperatures (a) for the thermal bridge Case 3 for three locations: Point [0.35; 0.35; 0.15] is located in the lower part of the insulation (EPS) corner; Point [0.5; 0.5; 0.05] is located inside the concrete part of the thermal bridge; Point [0.6; 0.5; 0.05] is located on the external (concrete) surface. Temperatures computed with OpenFoam are plotted with lines and the results of MCM are given with markers. The scaled numerical error (Eq. 24) with the MCM confidence intervals are given in (b); Rendering (c) in the visible spectrum (0.38-0.78 μm , CIE XYZ [34]) with HTRDR-Urban [33, 30] of the complex geometry: two parallel rows of five aligned buildings; The walls are Lambertian and the windows are specular; Solar elevation is 45° and azimuth is 120° from north (clockwise). An infrared geometry rendering is shown in (d) with reference radiance temperatures computed with HTRDR-Urban. In (e) the pixel-based scaled differences between the present model and the reference are given (each image has a resolution of 300×300 pixels)



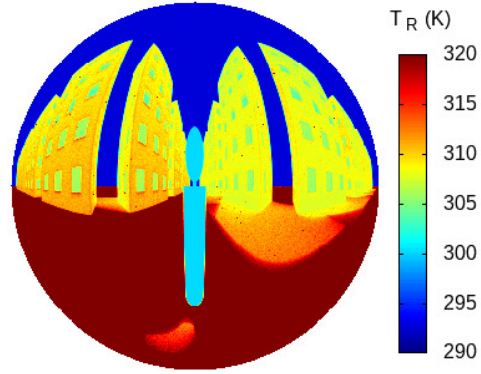
(a) Building lines with trees and centred body surface (S_b)



(b) Temporal evolution of air temperature and solar irradiances

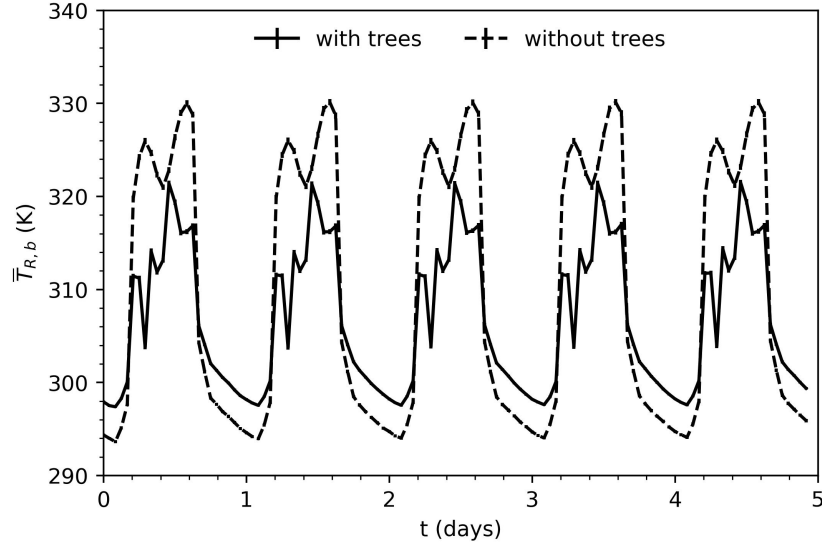


(c) Thermal environment accounting for trees

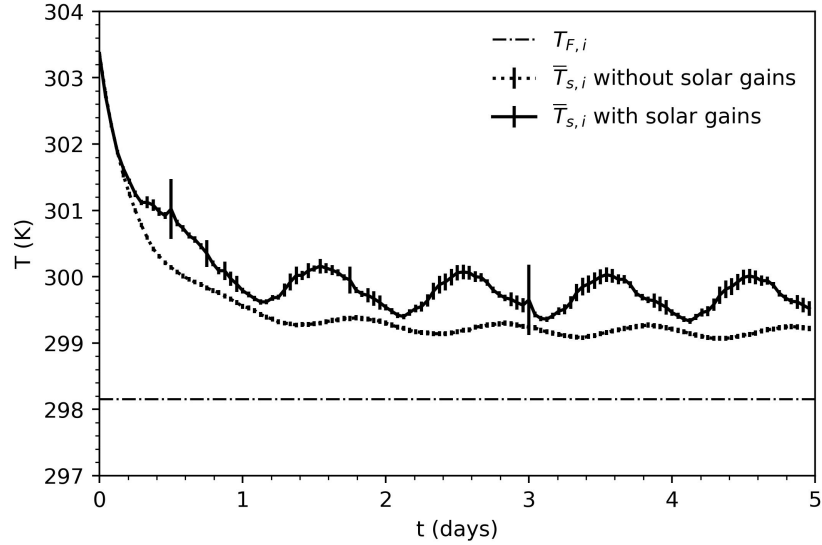


(d) Thermal environment without trees

Figure 6: Heat wave scenario geometry, five days weather data and radiative temperature mappings: (a) Representation of the building rows and of the centred body geometry; (b) Time evolution of the external air temperatures ($T_{F,e}$, Eq. 25) and solar direct (D_o) and diffuse ($H_{o,sky}$) irradiances; Mollweide projection of θ_R onto a disc computed with MCM giving the thermal environment around the body surface with (c) or without (d) trees for the heat wave scenario at 1 pm the first day (corresponding to $t \approx 0.54$ days). For each pixel $N = 10^3$ leading to $\sigma_{\bar{T}_R} \leq 0.4$ K for the buildings and $\sigma_{\bar{T}_R} \leq 0.8$ K for the ground



(a) Temporal MRT on the body surface during the heat wave scenario



(b) Temporal average internal wall temperature during the heat wave scenario

Figure 7: Temporal evolutions obtained with MCM during the heat wave scenario: (a) for the body surface MRT (Eq. 26) when trees are considered or not ($N = 10^5$, error bars are computed with $\pm 3 \sigma_{\bar{T}_{R,b}}$); (b) for the surface average internal wall temperature (Eq. 27) with or without the solar gains coming through the window glasses, ($N = 10^5$; error bars are computed with $\pm 3 \sigma_{\bar{T}_{s,i}}$, and the constant room air temperature, $T_{F,i}$, is also plotted)